JGR Atmospheres

RESEARCH ARTICLE
10.1029/2020JD033857

High-Resolution Observations of Turbulence Distributions Across Tropopause Folds

Jens Söder[1], Christoph Zülicke[1,2], Michael Gerding[1], and Franz-Josef Lübken[1]

[1]Optics Department, Leibniz Institute of Atmospheric Physics at the University of Rostock, Kühlungsborn, Germany, [2]Theory Department, Leibniz Institute of Atmospheric Physics at the University of Rostock, Kühlungsborn, Germany

Key Points:

- High-resolution turbulence measurements show severe (moderate) turbulence strength in deep (medium) tropopause fold
- Eddy heat fluxes are found to modify potential vorticity distribution across tropopause fold comparable to other studies
- Unexpectedly, in both cases dissipation rates above the jet are three orders of magnitude larger than below

Supporting Information:

- Supporting Information S1

Correspondence to:
J. Söder,
soeder@iap-kborn.de

Citation:
Söder, J., Zülicke, C., Gerding, M., & Lübken, F.-J. (2021). High-resolution observations of turbulence distributions across tropopause folds. *Journal of Geophysical Research: Atmospheres*, *126*, e2020JD033857. https://doi.org/10.1029/2020JD033857

Received 14 SEP 2020
Accepted 11 JAN 2021

Abstract In this study, we interpret two vertical turbulence measurements. We acquired these uninterrupted high-resolution dissipation rate profiles with the balloon-borne instrument LITOS (Leibniz Institute Turbulence Observations in the Stratosphere) from velocity measurements using a spectral technique. The meteorological situation is characterized using ECMWF's integrated forecast system (IFS) as breaking Rossby waves showing significant tropospheric jets and a developed tropopause fold. In both cases, dissipation rates in the shear zone above the upper-tropospheric jet are three orders of magnitude larger than below, reaching severe turbulence strengths (1,000 mW kg^{-1}) in a deep tropopause fold and moderate turbulence strengths in a medium tropopause fold (10 mW kg^{-1}). These turbulent spots are shown to create a tripole shaped pattern of PV modification across the tropopause. Furthermore, tracer-tracer correlations exhibit mixing of tropospheric and stratospheric air masses in the medium-fold case. While the strength of turbulence corresponds to the depth of the tropopause fold, its asymmetric vertical distribution is possibly related to the tropopause fold life cycle. The observed asymmetry in the vertical turbulence distribution is consistent across both tropopause folds and in overall agreement with measured Richardson numbers. In the medium-fold case however, it is neither expected from conceptual models nor from Richardson numbers in the IFS. This calls for further field campaigns to investigate the role of turbulence and its implications for the meteorological understanding as well as for aviation safety.

Plain Language Summary Tropopause folds are areas where air from higher altitudes is submerged under the jet stream. These areas are important for the vertical exchange of trace gases and are known for creating aviation hazards due to enhanced turbulence. In our study, we use high-resolution turbulence measurements from balloons to study the phenomenon. For further understanding, these observations are compared to data from weather forecast models. While we generally find a quantitative agreement between our measurements and other studies, the observed turbulence pattern is unexpected: we find turbulence strengths above the jet stream to be 1,000 times stronger than below. As conceptional models predict a strengthening of tropopause folds due to turbulence, this result has a likely influence on our understanding of the phenomenon as well as it highlights potential hazards for high flying passenger aircraft.

1. Introduction

Tropopause folds are regions where stratospheric air is submerged under the upper-tropospheric jet. In the extratropics, they are fundamental to the understanding of stratosphere-troposphere exchange processes and the strength of these processes is largely variable (e.g., Stohl et al., 2003). While the tropopause acts as a transport barrier most of the time, tropopause folds can be associated with strong exchange of trace species across this barrier (Holton et al., 1995; Shapiro, 1980). These folds have been discovered in the mid-twentieth century (Bjerknes, 1937; Reed & Danielsen, 1958), about 50 years after the discovery of the tropopause (Hoinka, 1997). For a detailed account on tropopause folds in terms of the history of the idea the reader is referred to Keyser and Shapiro (1986).

In order to give a good account of the tropopause region under such dynamical conditions, it is useful to apply a dynamical tropopause definition instead of a thermal one as given in WMO (1957). The dynamical description defines the tropopause as a quasi-material surface of constant potential vorticity (PV) (Holton et al., 1995; Hoskins, 1997). Generally, tropopause folds are part of upper-level jet-front systems (ULJFs), which are themselves part of the baroclinic wave life cycle (Bush & Peltier, 1994; Shapiro & Keyser, 1990).

The upper-level fronts are zones of enhanced vertical gradients of horizontal wind as well as enhanced horizontal temperature and PV gradients. Typical along-front scales are 1,000–2,000 km, while cross-front scales are one order of magnitude smaller (Keyser & Shapiro, 1986; Shapiro, 1981).

Rossby wave breaking events are a frequent phenomenon at midlatitudes—they occur in 40% of all winter days and they show tilted wave-like displacements of warm air toward the pole (Zülicke & Peters, 2008). These poleward extensions of subtropical air occur within *ridges*, i.e., regions of high geopotential (low potential vorticity), while the equatorward excursion of cold air masses occurs within *troughs*, i.e., regions of low geopotential (large potential vorticity) on isobaric (isentropic) surfaces. At either side of such a high-pressure ridge strong meridional transports are realized in ULJFs, bringing tropospheric air northward and upward at the western side and stratospheric air southward down at the eastern side of the ridge. The associated ageostrophic cross-frontal circulation gives rise to the formation of tropopause folds (Shapiro, 1981). This understanding of the tropopause fold as an effect of the ageostrophic circulation around the jet is most fundamental, while further extensions include effects of finite-size jet streaks and separate upper-troposphere and lower-stratosphere fronts (Lang & Martin, 2012) or adiabatic forcing (Spreitzer et al., 2019). This adiabatic forcing is partly generated by turbulence as first described by Shapiro (1976).

More specifically, ULJFs and tropopause folds in particular are a well-known source of turbulence due to their strong vertical gradients of horizontal wind (e.g., Koch et al., 2005; Shapiro, 1974; Sharman et al., 2012). The turbulence in turn drives mixing processes between tropospheric and stratospheric air (Cho et al., 1999; Holton et al., 1995; Lamarque & Hess, 1994). Turbulence generation in tropopause folds has been attributed to Kelvin-Helmholtz instabilities (e.g., Cho et al., 1999) as well as to convective sources (Koch et al., 2005; Reid & Vaughan, 2004). By generating turbulent potential temperature fluxes and therefore modifying the PV in ULJFs, turbulence is not only a consequence of strong frontal gradients, but acts frontogenetic itself (e.g., Keyser & Shapiro, 1986). Here the idea is that turbulent mixing in both shear layers creates an area of enhanced PV on the cyclonic side of the jet at the height of its core, which amplifies the above mentioned ageostrophic circulation around the jet (Shapiro, 1976). This has been confirmed by recent model studies using numerical weather forecasts and by two older, more conceptional 2D investigations (Chagnon & Gray, 2015; Gidel & Shapiro, 1979; Saffin et al., 2017; Shapiro, 1981; Spreitzer et al., 2019). Therefore, turbulence is expected to act frontogenetic by sharpening frontal gradients in the shear zones below the jet as well as above the jet (Shapiro, 1981, his Figure 17). This is counter-intuitive, because on smaller-scales, turbulent mixing leads to a weakening of gradients (e.g., Fritts & Werne, 2013, Figure 4).

Spreitzer et al. (2019) showed that shear driven turbulence in the frontal zones around the jet creates a tripole structure in PV. Saffin et al. (2017) and Chagnon and Gray (2015) observed the generation of a PV dipole with a maximum slightly above the dynamical tropopause. Even though the shape of the PV modification differs, all studies are in line with the conceptual picture given by Shapiro (1976). Generally, the enhanced dissipation rates are associated with eddy heat flux. The heat flux in turn induces a PV modification that is a function of its second vertical derivative. Consequently, we may expect a tripole of negative-positive-negative PV tendency for a single dissipation peak. When there are two dissipation peaks, for example above and below the upper-level jet, a pentapole structure would correspond. The particular form of this PV structure depends on the specific shape of the turbulence distribution. In the original model of Shapiro (1976), for example, both dissipation peaks above and below the jet are symmetric.

Furthermore, turbulent processes are important for the breakdown of tropopause folds. Without mixing processes tropopause folds are reversible. Only the formation of smaller scale filaments, their evolution to smaller and smaller scales by turbulence and finally molecular mixing at the smallest scales will lead to stratosphere-troposphere exchange (Hartjenstein, 2000; Stohl et al., 2003). This means that turbulence in tropopause folds does not only act frontogenetic, but it also plays a vital role in the mixing of trace gases across the tropopause. In the last two decades, several mostly aircraft based studies on trace gas distributions in tropopause folds have been performed (Cho et al., 1999; Gettelman et al., 2011; Pan et al., 2007; Ungermann et al., 2013; Woiwode et al., 2018). Typically, they use correlations of two tracers, one of which has high stratospheric and the other one high tropospheric abundance. The tracer-tracer correlation is then used to identify tropospheric and stratospheric air masses as well as well mixed regions that are frequently called *extratropical transition layer* (Gettelman et al., 2011). For our study, these tracer-tracer correlations allow to assess whether mixing has taken place at a previous stage of the tropopause fold development.

Earlier conceptional models described the front in an ULJF as one continuous zone reaching from the upper troposphere up into the lower stratosphere on the cyclonic side of the jet core (e.g., Shapiro, 1976). More recently however, Lang and Martin (2012) showed that they are best described by separating them into a upper tropospheric (UT) front below the upper-level jet and a lower stratospheric (LS) front above the jet, which has already been partly suggested by Shapiro (1981). More specifically, the ageostrophic circulation in the ULJF acts frontogenetic or frontolytic on either of the frontal zones, depending on the stage of the frontal development and their position with respect to the baroclinic wave (Lang & Martin, 2012).

Since the 1970s, aircraft-based observational studies in tropopause folds have been performed. Some of them derived kinetic energy dissipation rates as a measure for turbulence strength (Cho et al., 1999; Kennedy & Shapiro, 1975, 1980). However, among these there is only one turbulence sounding in the upper shear layer of the tropopause jet (Kennedy & Shapiro, 1980). All the others took place in the shear layer below the jet or at the height of its core. Altogether, these studies consist of single measurements, but are not able to provide a complete altitude profile of turbulence. Furthermore, Reid and Vaughan (2004) used a radar to derive energy dissipation rates in the UT front of a tropopause fold while some others did not report quantitative dissipation rates but air traffic related qualitative classifications for turbulence intensity such as *moderate or greater* (e.g., Koch et al., 2005; Shapiro, 1976).

In conclusion, we state that the aforementioned explanation of turbulence influence on tropopause fold generation by Shapiro (1976) expects turbulence to occur in the UT front as well as in the LS front (their Figure 17). Quantitative observations of turbulence however, are almost exclusively available for the UT front.

We intend to bridge this gap by performing high-resolution in situ soundings of turbulent energy dissipation rates, which are used to deduce eddy heat fluxes and PV tendencies across tropopause folds. State of the art aircraft based studies allow for reliable determination of energy dissipation rates (Bramberger et al., 2017; Strauss et al., 2015). However, aircraft measure mainly horizontal transects trough tropopause folds and their operational costs are high, especially for larger altitudes. Radar based techniques to determine energy dissipation rates usually show a coarser spatial resolution (e.g., Hocking & Mu, 1997).

Therefore, we used the balloon-borne instrument LITOS (Leibniz Institute Turbulence Observations in the Stratosphere) to acquire high-resolution turbulence profiles in tropopause folds (Schneider et al., 2017; Theuerkauf et al., 2011). It infers kinetic energy dissipation rates from velocity fluctuations by fitting the Taylor microscale that separates the inertial from the viscous subrange of turbulence (Lübken, 1992; Heisenberg, 1948). For this study, we use the latest version of the instrument measuring on a descending balloon in the unperturbed flow below the gondola. Thereby, we are able to avoid any influence from the balloon's wake (Kräuchi et al., 2016; Söder et al., 2019).

In summary, we will use our LITOS data to answer the following research question:

Is there observational evidence for the turbulence distribution proposed by Shapiro (1976) and if not, is the observed structure in agreement with state-of-the-art interpretations of tropopause fold development?

We will give a brief description of the LITOS instrument flown together with a radiosonde as well as of the operational weather forecast data used for the interpretation (Section 2). Thereafter, the meteorological conditions of both tropopause fold observations are presented in Section 3. Furthermore, we discuss our turbulence observations and compare them to other dissipation rate measurements in tropopause folds. Furthermore, we relate our radiosonde measurements to the operational forecast (Section 4). As the main part of this paper, we will assess the conditions that lead to turbulence in the ULJF as well as the influence of turbulence on PV and tracer-tracer profiles in Section 5. Our study is summed up by a discussion of the results and a conclusion (Sections 6 and 7, respectively).

2. Data and Methods

2.1. LITOS Turbulence Data

LITOS uses a constant temperature anemometer to measure turbulent fluctuations in the atmospheric velocity field (Theuerkauf et al., 2011). We use two balloons for the ascent and cut one of them away at the top altitude. The remaining balloon is filled such that the payload sinks down at approximately 5 m s^{-1} (Kräuchi

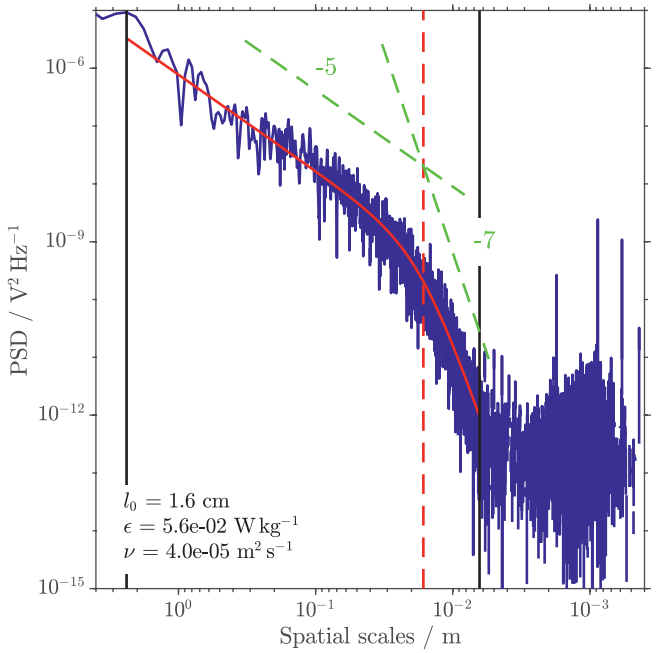

Figure 1. Exemplary spectrum of LITOS data from January 19, 2020, 10,927–10,944 m. PSD from raw data shown in blue together with fit following the Heisenberg (1948) equation (solid red), inner scale l_0 (dashed red), fit range (solid black) as well as slope of inertial (−5/3, light green) and viscous subrange (−7, light green). ε denotes the retrieved energy dissipation rate and ν the kinematic viscosity. LITOS, Leibniz Institute Turbulence Observations in the Stratosphere; PSD, power spectral density.

et al., 2016). The gondola is located 120 m below the balloon and the sensor measures in the unperturbed flow below the gondola, avoiding any wake influence (Söder et al., 2019).

In order to retrieve the energy dissipation rate ε, we divide the velocity fluctuation measurement into time bins of 5 s, and calculate the power spectral density (PSD) using a modified version of Welsh's method (Attivissimo et al., 2000). This corresponds to an altitude resolution of the turbulence retrieval of approximately 25 m. As a first step, we automatically detect the power of the instrumental noise for each time bin and subtract it from the measured spectrum (small-scale end of the exemplary spectrum in Figure 1). Then we fit the Heisenberg (1948) spectrum of turbulence to the spectral data. This model contains the Taylor microscale l_0 as a free parameter, separating the inertial (slope −5/3) from the viscous subrange (slope −7) of turbulence. Subsequently, the fit quality is scrutinized according to the following criteria to sort out nonturbulent and technically distorted spectra:

1. The noise level detection must not fail
2. The fitting routine has to terminate
3. The width of the fit range has to be at least one order of magnitude
4. The Taylor microscale l_0 has to be within the fit range
5. The root mean square distance between the data and the fit must not be larger than 0.3 orders of magnitude
6. The slope at the small-scale end of the fit range has to be at least −4

Subsequently, all valid fits are used to calculate energy dissipation rates according to Lübken (1992) and Schneider (2015):

$$\varepsilon = c_{l0}^4 \frac{\nu^3}{l_0^4}. \quad (1)$$

$c_{l0} = 15.8$ is a constant adapted to our measurement geometry, which is sensitive to one longitudinal and one transversal direction (Schneider et al., 2017). ν is the kinematic viscosity of the background flow calculated according to NOAA (1976) from the radiosonde data (cf. Section 2.2). Figure 1 shows a typical example for such a turbulent velocity spectrum from the data taken on January 19, 2020.

This implies that in the LITOS retrieval we regard those and only those cases as turbulent that allow for a reliable determination of the dissipation rate ε. These altitude bins are shown by a blue circle in the dissipation rate profile shown in Figure 4. The measurement from January 19, 2020 has been performed with a revised version of the instrument where the noise level of the electronics has been reduced by a factor of four compared to the older version used on August 6, 2016. For a more detailed description of the dissipation rate retrieval, the quality control procedures, and a comparison with another turbulence measuring instrument, please see Söder (2019).

Our technique of fitting the Taylor microscale l_0 only uses spatial scales smaller than 2 m, thereby avoiding influences from turbulence, self-induced balloon motions, pendulum motions of the gondola, and internal oscillations of the balloon (Scoggins, 1967; Söder, 2019; Tiefenau & Gebbeken, 1989). Furthermore, it only relies on the spectral shape of the measurement data, not on the absolute value of the fluctuations, thereby avoiding a complicated calibration (Theuerkauf et al., 2011; Xie et al., 2017).

At higher altitudes, constant temperature anemometer measurements may be affected by a damping of the transfer function at high frequencies (Jørgensen, 2005; Li, 2004; Xie et al., 2017). Therefore, we restrict our data evaluation to Knudsen number below $Kn = 0.1$ in order to avoid influences on the retrieved dissipation rates (Söder, 2019). This corresponds to an altitude limit of approximately 17.5 km.

2.2. Radiosonde Data

A Vaisala RS-41 radiosonde is mounted upside-down between the balloon and the gondola on the LITOS instrument (Survo et al., 2014). We use it to retrieve wind, temperature, and humidity for the geophysical part of our study and to calculate the kinematic viscosity according to NOAA (1976). The latter is used in the LITOS retrieval (Theuerkauf et al., 2011). The temporal resolution of the data output is 1 s. The manufacturer of the radiosonde reports uncertainties in pressure, temperature, relative humidity and wind speed of $\Delta p = 1$ hPa, $\Delta T = 0.3$ K, $\Delta\mathrm{RH} = 4\%$ and $\Delta U = 0.15$ m s^{-1} at the height of the tropopause. For pressure, temperature and relative humidity the precision is half of the uncertainty, while it is not stated for wind speed (Vaisala, 2018). Compared to standard measurements on ascending balloons, the sounding on descent avoids influences on the radiosonde temperature and humidity measurement from the balloons wake that is heated due to solar heating of the balloon's skin (Kräuchi et al., 2016; Söder et al., 2019; Tiefenau & Gebbeken, 1989).

During the measurement of our first case, we lost data connection to the radiosonde on descent in an altitude of 9,100 m due to obstacles in the line of sight from LITOS to the ground station. However, the whole flight distance above ground was only 190 km, being short compared to typical along-front scales of 1,000 to 2,000 km (e.g., Keyser & Shapiro, 1986). Therefore, we took the upleg data for the altitude range below 9,100 m. We do not expect any significant influence from our decision to combine descent and ascent data, which is reflected in a gap between the ascent and descent data of only $T = 0.6$ K, RH = 1.4 %, and $U = 1$ m s^{-1}. The turbulence retrieval was not affected by this issue, because the LITOS data are stored on-board.

2.3. Operational Forecast Data

The Integrated Forecast System (IFS) of the European Center for Medium-Range Weather Forecasts (ECMWF) is used for two-dimensional plots of the meteorological conditions. The IFS is a global, hydrostatic numerical weather prediction model. The calculations are done on a T1279 spectral grid (equal to about 0.073° grid spacing) with hybrid sigma-pressure levels. For our study, we use the HRES output, cycle 45r1. It provides hourly forecasts on 137 pressure levels with a horizontal resolution of 0.25°. In the target region, this corresponds to a latitudinal grid spacing of 28 km and a longitudinal grid spacing of 17 km. The vertical resolution at the height of the jet cores is about 290 m.

IFS fields are compared to radiosonde data measured on the LITOS payload (not assimilated in the forecast). For this comparison, the forecast time closest to the measurement is chosen and the model data are linearly interpolated in space onto the flight path of the LITOS instrument.

In this study, we use an iso-surface of potential vorticity (PV) as the dynamical tropopause (Hoskins et al., 1985). PV is defined as:

$$\mathrm{PV} = -g\left(\zeta_\theta + f\right)\partial\theta \,/\, \partial p, \tag{2}$$

where g denotes gravitational acceleration, ζ_θ the relative vorticity on potential temperature isosurfaces, f the planetary vorticity, and $\partial\theta/\partial p$ the pressure gradient of potential temperature. In the literature, values for the dynamical tropopause vary from 1 PVU to 4 PVU (1 PVU $\doteq 10^{-6}$K m^2 kg^{-1} s^{-1}). We use a threshold of 2 PVU in order to be consistent with several publications (e.g., Holton et al., 1995; Pan et al., 2007; Spreitzer et al., 2019; Woiwode et al., 2018).

3. Meteorological Conditions

Both LITOS measurements where performed above Northern Germany. After being launched at the Institute of Atmospheric Physics in Kühlungsborn (IAP), the balloon drifted mainly south-westward on January 19, 2020 (south-eastward on August 6, 2016) and the measurement phase lasted from 15:14 UT to 17:04 UT (14:01 UT to 15:31 UT). In order to visualize the meteorological conditions during both measurements,

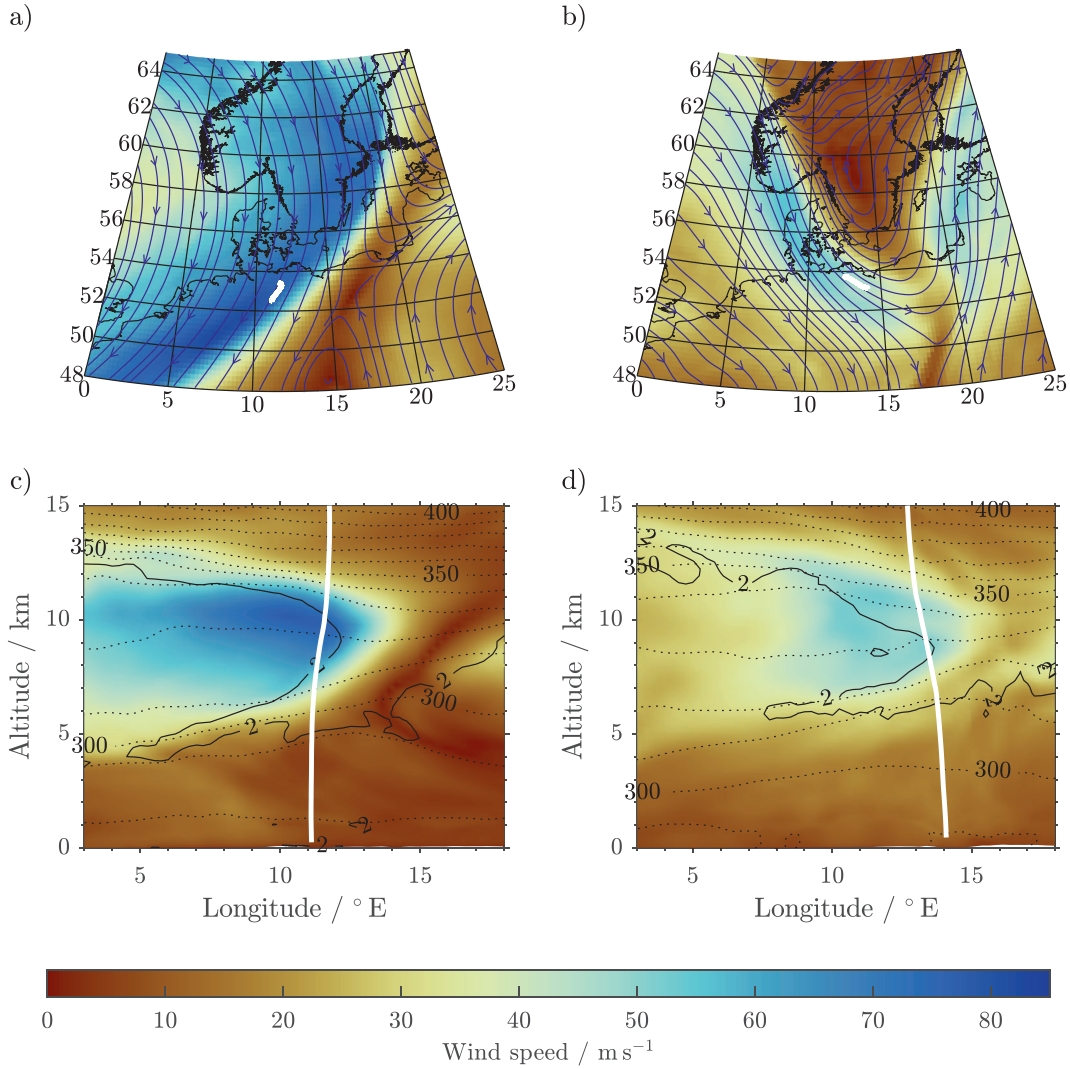

Figure 2. (a) Map of horizontal wind speed at 10 km altitude on January 19, 2020, 16 UT from the IFS (deep-fold case). Stream-lines of the horizontal wind are given in blue. (b) Same for the measurement from August 6, 2016 (medium-fold case, IFS: 15 UT). (c and d) Same as above, but showing a longitudinal section of the IFS data at the latitude, where the balloon crossed the tropopause fold (53.05°N for deep-fold and 53.48°N for the medium fold case). Potential temperature is shown by dotted isolines, the dynamical tropopause at 2 PVU by a solid black line. In all panels, the LITOS flight path is denoted by a solid white line. All colorbars used in this study are given by Crameri et al. (2020).

wind speed, lines of constant potential temperature (isentropes) and the height of the dynamical tropopause as given in the IFS are shown in Figure 2 for 16:00 UT (15:00 UT).

The synoptic situation during both LITOS campaigns is driven by the evolution of a baroclinic wave. Here we give a brief summary of a subjective analysis in the supporting information: The 2020 case is associated with a Rossby wave breaking event inducing strong tropospheric jets (80–90 m s^{-1}) and a far northward extension of the ridge (70°N to 73°N). This supposes a strong import of stratospheric air at the eastern flank of the ridge. The tropopause fold reaches as low as 4.0 km and can be classified as *deep* (Škerlak et al., 2015; Sprenger et al., 2003). The 2016 event Rossby wave breaking event is weaker: this regards the jet speed (40–50 m s^{-1}), the extension of the ridge (63°N to 70°N) and the tropopause fold that is classified as *medium*. The measurement took place in the jet exit region south-westward of a trough. Plots supporting these classifications and further details of the upper-level jet-front systems (ULJFs) are shown in the Figures S1–S4.

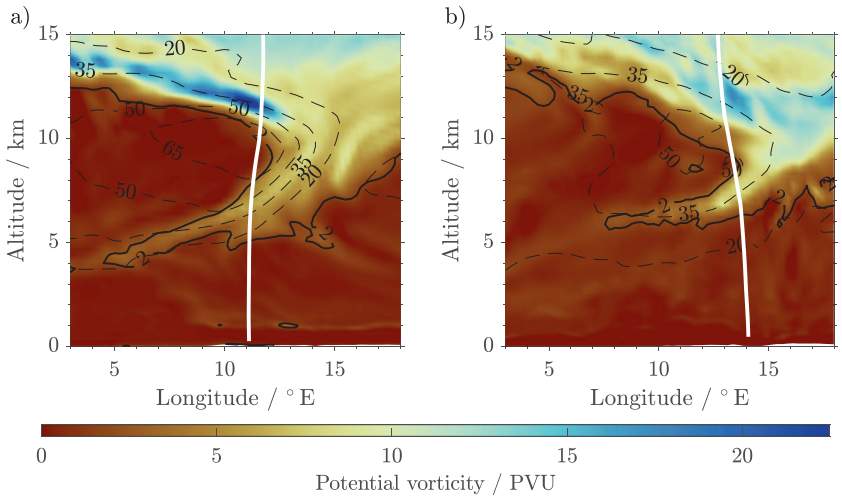

Figure 3. Same as Figures 2c and 2d, but showing potential vorticity from the IFS. Lines of constant wind speed are marked in dashed black, the dynamical tropopause in solid black (2 PVU). IFS, integrated forecast system.

Both cases show a narrowing and tilting of the isentropes above the jet as well as below (Figures 2c and 2d). These areas are the lower stratospheric (LS) and the upper tropospheric (UT) front associated with the ULJF (Lang & Martin, 2012; Shapiro, 1981). They are characterized by strong horizontal temperature and vertical wind gradients as well as by static stability (Keyser & Shapiro, 1986). While the dynamical tropopause on the anticyclonic (western) side of the jet is at about 13 km altitude, it comes down to about 6 km on the cyclonic (eastern) side while its height increases again further to the east.

According to Lang and Martin (2012), ULJFs follow a distinct life cycle, depending on their location in the baroclinic wave. Both measurements discussed in this study were located on the eastern side of a ridge. Lang and Martin (2012) found for this location of ULJFs the LS front to have stronger gradients than the UT front at the beginning of the development. The resulting ageostrophic circulation acts frontolytic in the LS front and frontogenetic in the UT front according to Lang and Martin (2012). This leads to an earlier decay of the LS front compared to the UT front.

For our case from January 19, 2020 frontal gradients in the ULJF are seen in the IFS to last for several 10 h after the measurement (Figure S5). Gradients were increasing in the UT front and decreasing in the LS front on time scales of a few hours. Conversely, on August 6, 2016 most of the frontal features vanished within 12 h after the sounding (Figure S6). Furthermore, the IFS shows stronger gradients in the UT front compared to the LS front. For a discussion of the frontal gradients as measured by the radiosonde, please see Section 5.1.

In both cases that are discussed here a submersion of PV rich stratospheric air under the jet from the cyclonic side of the baroclinic wave is observed (Figure 3). The tongue of stratospheric air reaches down to altitudes of about 4 km in the deep-fold case and 6 km in the medium fold case at the time of our measurement.

In many cases, tropopause folds have been observed to be accompanied by gravity waves generated from imbalances in the large-scale flow (Koch et al., 2005; Zhang, 2004; Zülicke & Peters, 2006) or flow over topography (Woiwode et al., 2018). In our cases however, no significant gravity wave activity is seen neither in the IFS data nor in the radiosonde measurements (presented in Section 4.2).

4. In Situ Measurements

4.1. Turbulence Measurements

The most prominent feature of both the deep-fold case (January 19, 2020) and the medium-fold case (August 6, 2016) is a peak in dissipation rate centered around 10.4 and 11.2 km altitude, respectively. Both profiles are shown in Figure 4, with peaks located in the shear zone above the jet (centered around 9.5 km altitude) within the LS front.

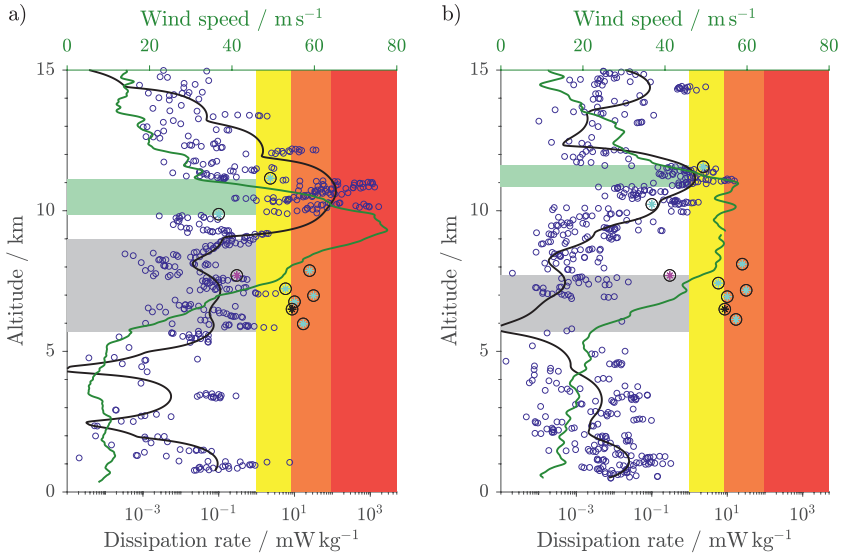

Figure 4. (a) Turbulence profile from January 19, 2020 (deep-fold case). (b) Turbulence profile from August 6, 2016 (medium-fold case). Both: each blue circle marks a turbulent altitude bin, the solid black line a 2 km running average and the solid green line shows the wind speed for reference. Color shading indicates light, moderate, and severe turbulence (yellow, orange, and red) according to ICAO (2018), as well as the height of the dissipation rate peak (green) and the height of the stratospheric intrusion (gray). Turbulence measurements under similar conditions are taken from Reid and Vaughan (2004, black star), Cho et al. (1999, magenta star), and Kennedy and Shapiro (1980, cyan stars).

In the deep-fold case (Figure 4a), the peak dissipation rate reached ~1,000 mW kg^{-1}. This dissipation strength corresponds to *severe* turbulence encounters in the classification of ICAO (2018). There is a sharp transition from the low dissipation rates underneath the jet (~0.1 mW kg^{-1}) to the LS peak. In contrast, the upper edge of this peak shows a smooth decay of dissipation rates down to ~0.1 mW kg^{-1} within 4 km. Furthermore, there is a slight enhancement in dissipation rates below the jet in the UT front in altitudes between 6 and 8 km up to *light* turbulence in the classification of ICAO (2018).

In the medium-fold case (Figure 4b), peak dissipation rates reached ~10 mW kg^{-1}, corresponding to *moderate* turbulence encounters (ICAO, 2018). The shape of the dissipation peak was opposite to that measured in the first campaign: sharp transition above the jet and a smooth one below. Furthermore, there is a *light* peak around 14.3 km altitude, which could not be related to the meteorological situation. It may be decaying turbulence that is advected from another place.

Quantitative turbulence soundings in the vicinity of tropopause folds are rare. For comparison, reported dissipation rates are plotted along with the LITOS measurement in Figure 4. Reid and Vaughan (2004) examined a tropopause fold where mixing by convection reaching into the frontal zone was observed by radar and aircraft data. Both measurements revealed dissipation rates around 10 mW kg^{-1}. Reid and Vaughan (2004) furthermore examined turbulence in 16 tropopause folds without convection. They found dissipation rates of less than 10 mW kg^{-1}. Cho et al. (1999) as well as Kennedy and Shapiro (1980) used wind in-situ measurements from research aircraft to deduce energy dissipation rates.

4.2. Comparison Between Radiosonde and Forecast Data

Figure 5 shows radiosonde data from the LITOS payload as well as IFS data interpolated onto the flight path. This comparison is done in order to establish if and in which regions the IFS data agree with our radiosonde data and can therefore be used for a quantitative comparison with the turbulence measurements.

For the deep-fold case (January 19, 2020, Figure 5a), IFS wind and potential temperature fields generally show good agreement with the radiosonde measurements. Deviations are typically below ±5 m s^{-1} and 4 K, respectively. Nevertheless, the vertical thickness of the tropopause jet is slightly overestimated in the IFS, leading to deviations in wind speed of up to 20 m s^{-1} at these altitudes. Furthermore, potential temperatures

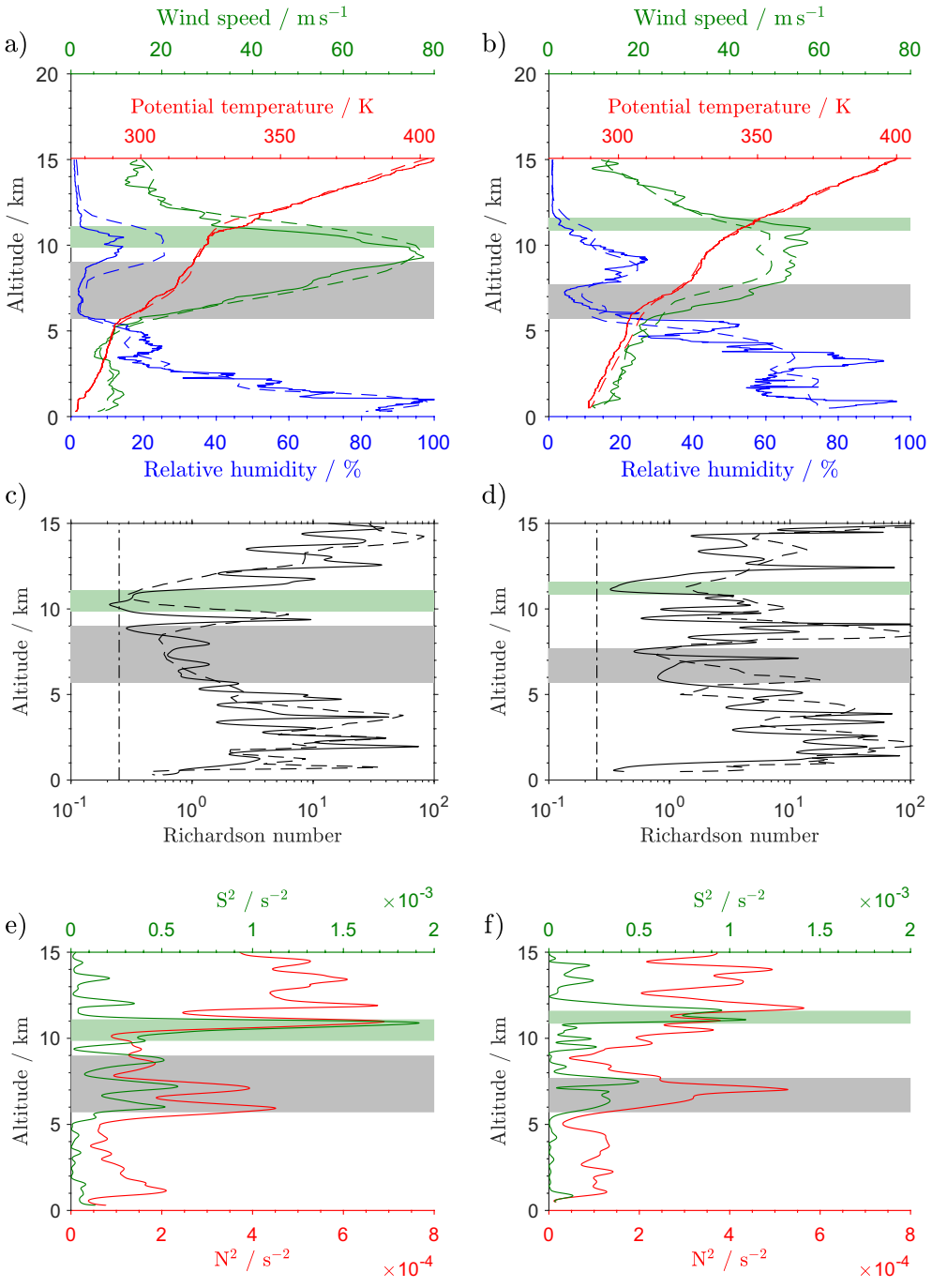

Figure 5. (a) Wind speed, potential temperature and relative humidity as measured by the radiosonde on board of the LITOS payload during the deep-fold case (January 19, 2020, solid lines). Dashed lines show values from the IFS interpolated to the flight path of the LITOS instrument. (c) Richardson numbers calculated from the radiosonde (solid) and from the IFS (dashed). (e) Squared static stability (red) and squared wind shear (green) measured by the radiosonde. (b, d, and f) Same as (a, c, and e), but for the medium-fold case (August 6, 2016). Gray color shading indicates the altitude range of the stratospheric intrusion, green color shading that of the peak in dissipation rate as marked in Figure 4. IFS, integrated forecast system; LITOS, Leibniz Institute Turbulence Observations in the Stratosphere.

differ by up to 9 K in the upper shear region of the jet. The humidity measurement agrees well with the forecast, except for the altitudes directly above the tropopause. Here the model overestimates relative humidity roughly by a factor of two. This is consistent with other studies finding a moist bias of the IFS in the lowermost stratosphere compared to observations (Kaufmann et al., 2018; Woiwode et al., 2020). Below the stratospheric intrusion some filamentation on vertical scales of about 1 km is poorly resolved by the IFS.

Likewise, the radiosonde measurement from the medium-fold case (August 6, 2016) is consistent with IFS data in general (deviations below ±5 m s^{-1} and 3 K, respectively). However, the wind magnitude of the tropopause jet is underestimated in the model by about 10 m s^{-1}. Furthermore, the vertical extent of the jet is slightly too small in the model, leading to a local underestimation of winds speeds by ∼15 m s^{-1}. The humidity from the model agrees well with the measurement on larger scales but does not reproduce strong humidity filaments on vertical scales of ∼1 km.

5. Role of Turbulence in the Tropopause Fold

5.1. Flow Stability in the Upper-Level Jet-Front System

In this study, Richardson numbers (*Ri*) are used to quantify the flow stability in the ULJF:

$$Ri = \frac{N^2}{S^2}, \tag{3}$$

where N^2 is the squared Brunt-Vaisala frequency and S^2 the squared vertical shear of the horizontal wind. In order to avoid influences from measurement uncertainties, radiosonde data are smoothed using a 1 km Hann weighted average prior to the calculation of *Ri*. This is similar to common radiosonde data treatments, such as Kohma et al. (2019) using a low-pass filter with a cut-off length of 600 m.

In both observed cases the radiosonde measurement reveals a *Ri* minimum in the LS front, reaching $Ri = 0.21$ in the deep-fold and $Ri = 0.32$ in the medium-fold case (cf. Figures 5c and 5d). Both values are close to the classical criterion for dynamic instability of $Ri \leq 0.25$ (e.g., Werne & Fritts, 1999). In both UT fronts the minimum Richardson number is about three times higher than in the LS front. This points into the same direction as the LITOS measurements: in both cases turbulent dissipation rates in the LS front are about three orders of magnitude higher compared to the UT front (Figure 4).

As mentioned above, we use IFS data to obtain sections of *Ri* and other variables. Therefore, Figure 5 also shows a profile of *Ri* interpolated on the flight path in order to discuss the applicability of the model data. For the deep-fold case, the IFS shows a picture similar to the measurement with *Ri* being twice as high below the jet compared to above the jet. By contrast, during the medium-fold case Richardson numbers in the IFS are slightly below the jet compared to above. This would be consistent with expectations by Lang and Martin (2012) for the early and late development stages of ULJFs. However, Figure 5b reveals that this discrepancy is caused by the IFS underestimating the magnitude of the wind speed in the jet and thereby underestimating S^2 above the jet. Additional information on the time development of *Ri* in the IFS can be found in Figures S5 and S6. Furthermore, it is noted that in both cases the minimum Richardson number of the UT front is found at the top of the stratospheric intrusion.

Separating *Ri* into wind shear and static stability, we find for the deep-fold case that the shear in the LS front is about three times larger than in the UT front, while this ratio is reduced to a factor of two in the medium fold case (Figures 5c and 5d). For the medium-fold case, the static stability shows stratospheric values in the intrusion, while it is less enhanced in the deep-fold case. Both cases show a strong gradient in static stability across the dissipation rate peak.

5.2. Turbulence Driven Vertical Heat Fluxes

Turbulence acts on the frontal circulation by vertical flux of turbulent momentum $F_U = \overline{w'U'}$ and potential temperature $F_\Theta = \overline{w'\Theta'}$ (Keyser & Shapiro, 1986; Shapiro, 1981). In order to stay consistent with the early publications, we will define these vertical fluxes in altitude coordinates, while all derivatives are taken with

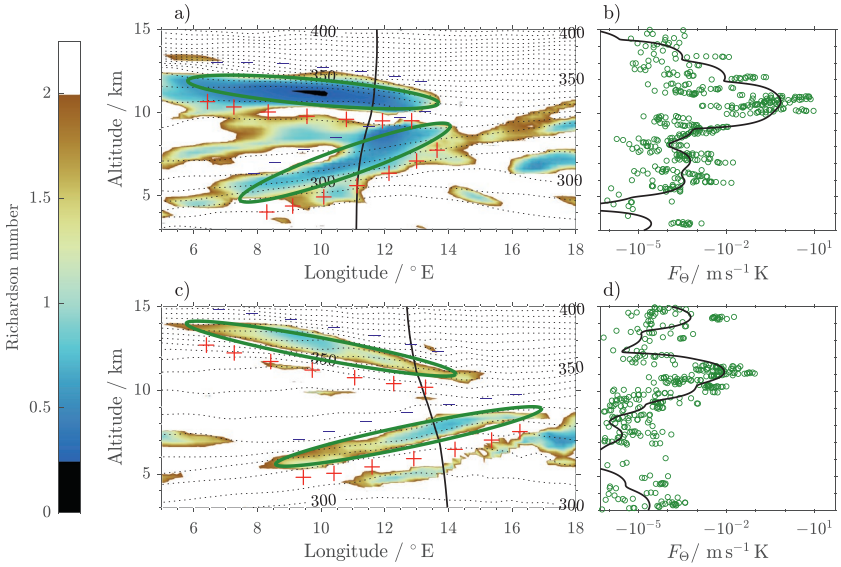

Figure 6. (a) Longitudinal section of Richardson numbers taken from the IFS for the deep-fold case (January 19, 2020, 16 UT). The LITOS flight path is denoted by a solid black line, isentropes are shown in dashed black. Green ellipses mark regions where increased vertical heat flux is expected with the corresponding temperature tendencies marked by red *plus* and blue *minus* signs ([a] Shapiro, 1976, his Figure 18). (b) Same as Figure 4, but showing vertical eddy flux of potential temperature for the deep-fold case (January 19, 2020). (c and d) Same as (a and b) but for the medium-fold case (August 6, 2016, 15 UT). IFS, integrated forecast system; LITOS, Leibniz Institute Turbulence Observations in the Stratosphere.

respect to pressure. Assuming stationary turbulence and neglecting third-order turbulent fluxes, the budget of turbulent kinetic energy in a horizontally homogeneous environment is given by:

$$\rho g F_U \frac{\partial U}{\partial p} + \frac{g}{\theta} F_\Theta = \varepsilon \tag{4}$$

(e.g., Zilitinkevich et al., 2008, Equation 2). This takes into account turbulence generation by work against the shear and by changes in potential energy through the potential temperature flux. The flux Richardson number is given as the ratio of the buoyancy and the negative shear term of Equation 4:

$$R_f = -\frac{1}{\rho\Theta} \frac{F_\Theta}{F_U \frac{\partial U}{\partial p}}. \tag{5}$$

We may eliminate the mechanical work (Reynolds) term and find a relation between the potential temperature flux and dissipation as

$$F_\Theta = -\frac{R_f}{1 - R_f} \frac{\Theta}{g} \varepsilon \tag{6}$$

(Lilly et al., 1974; Osborn, 1980). Lilly et al. (1974) assumed $R_f = 0.25$, while Osborn (1980) argued from oceanographic studies that steady state turbulence is characterized by $R_f \approx 0.15$. Zilitinkevich et al. (2008) have shown from a review of several experimental and numerical studies that the flux Richardson number increases with *Ri* and asymptotically approaches 0.2 when *Ri* exceeds 0.25. This is the *Ri* range that occurred in the turbulent shear zones sounded by LITOS (cf. Figure 5). However, the change in R_f results only in a slight modification of F_Θ compared to the variation of ε over several orders of magnitude. Therefore, we will neglect this dependence and use $R_f = 0.15$, corresponding to $Ri = 0.25$. Therewith, we can calculate eddy fluxes of potential temperature from energy dissipation rates by:

$$F_\Theta \approx -\frac{\Theta}{6g}\varepsilon. \tag{7}$$

Figures 6a and 6c show the LS front and the UT front for both cases as expected in the literature (Keyser & Shapiro, 1986; Lang & Martin, 2012). This means that reduced *Ri* are found in the shear zones, which hints at the occurrence of turbulence in these regions. The plus and minus signs indicate heating and cooling due to the expected turbulent redistribution of potential temperature according to

$$\frac{d\Theta}{dt} = g\frac{\partial}{\partial p}\left(\rho F_\Theta\right) \tag{8}$$

(Keyser & Shapiro, 1986).

The eddy heat flux derived from the LITOS dissipation rate measurement according to Equation 7 shows a different picture however: we only find significantly enhanced values in the LS front (Figures 6b and 6c). This is matching with the radiosonde measurement showing lower *Ri* for both cases in the LS front compared to the UT front, contrary to *Ri* in the IFS (cf. Section 5.1).

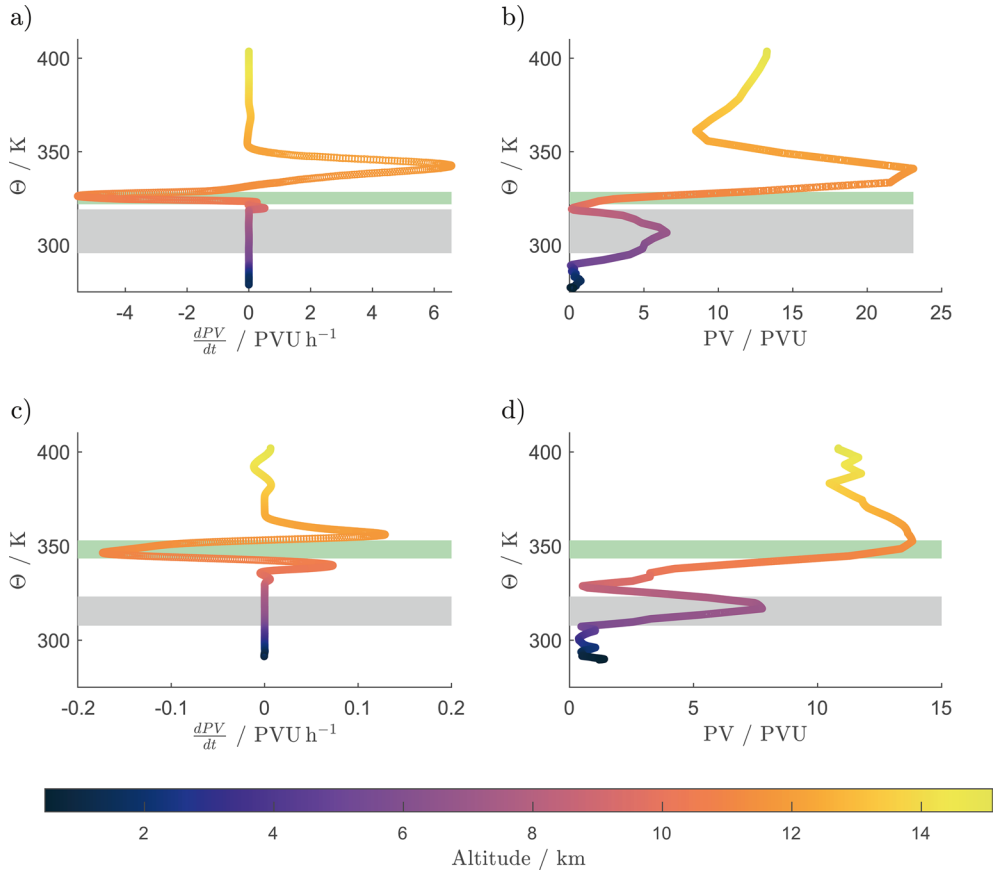

Figure 7. Left: PV source function derived from LITOS measurement and IFS data according to Equation 10 for the deep-fold case (January 19, 2020, [a]) and the medium-fold case (August 6, 2016, [c]). Right: Potential vorticity in the IFS interpolated on the LITOS flight path for the deep-fold case (b) and the medium-fold case (d). All: color shading showing turbulence peak in green and stratospheric intrusion in gray as in Figure 5. IFS, integrated forecast system; LITOS, Leibniz Institute Turbulence Observations in the Stratosphere; PV, potential vorticity.

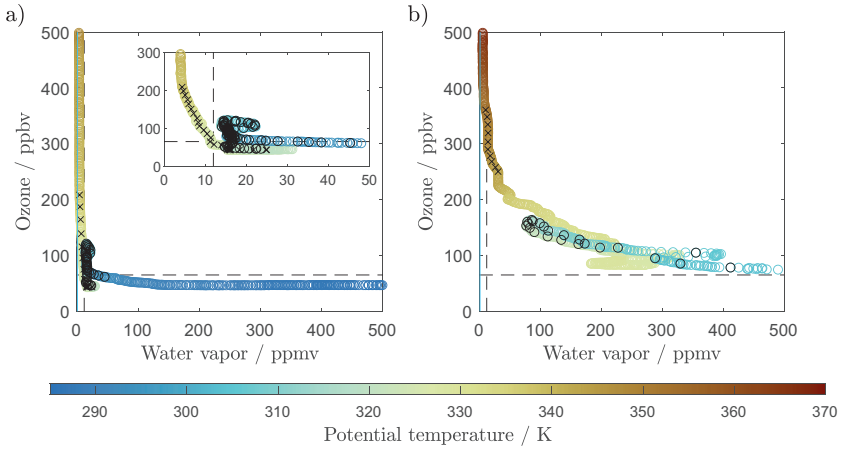

Figure 8. Tracer-tracer correlation of ozone and water vapor along the LITOS flight path for the deep-fold case (January 19, 2020, [a]) and for the medium-fold case (August 6, 2016, [b]). Water vapor data are taken from the radiosonde measurement, ozone from the IFS. Dashed black lines mark the lower ozone and lower water vapor limits of stratospheric and tropospheric air masses, respectively (ozone > 65 ppbv, water vapor > 12 ppmv). All: Crosses mark the height range of the turbulent peak in the LS shear zone, black circles that of the stratospheric intrusion (cf. Figure 5). The inset in (a) is made in order to enhance visibility of low trace gas concentrations in the tropopause region. IFS, integrated forecast system; LITOS, Leibniz Institute Turbulence Observations in the Stratosphere.

5.3. PV Modification by Eddy Heat Flux Convergence

In order to allow for a quantitative comparison of turbulence induced PV changes with other studies, we will use a concept developed by Shapiro (1976) to derive the source function for PV. Please note that in contrast to Shapiro (1976) our definition of PV is multiplied by the gravitational constant g (Equation 2).

Generally, PV is a conserved quantity on isentropic surfaces for adiabatic and frictionless motions (Holton et al., 1995; Hoskins et al., 1985). Neglecting diabatic and frictional heating, Shapiro (1976) found for the continuity equation of PV:

$$\frac{d\mathrm{PV}}{dt} = -g\frac{d}{dt}\left(\zeta_\theta + f\right)\frac{\partial\Theta}{\partial p} \approx -g\left(\zeta_\theta + f\right)\frac{\partial}{\partial p}\left(\frac{d\Theta}{dt}\right). \tag{9}$$

Combining Equations 8 and 9 leads to the prognostic equation of PV changes due to turbulent heat flux:

$$\frac{d\mathrm{PV}}{dt} \approx -g^2\left(\zeta_\theta + f\right)\frac{\partial^2}{\partial p^2}\left(\rho F_\Theta\right) \tag{10}$$

(Keyser & Shapiro, 1986). The final result is a relation between PV tendency and curvature of the dissipation profile, transformed to geometrical coordinates:

$$\frac{d\mathrm{PV}}{dt} \approx \frac{\Theta}{\rho g}\left(\zeta_\theta + f\right)\frac{R_f}{1-R_f}\frac{\partial^2\varepsilon}{\partial z^2}. \tag{11}$$

The turbulent PV modification obtained from the LITOS dissipation measurement on an isentropic coordinate is shown in Figure 7. We use potential temperature as vertical axis in order to magnify the steady increase in PV with potential temperature outside the folded structures as well as in order to be consistent with Figure 8. For the calculation according to Equations 7 and 10 we use the smoothed dissipation rates shown in Figure 4 and apply the same smoothing before each derivation in order to avoid influences of small-scale instrumental or atmospheric fluctuations on the result. Absolute vorticities used in Equation 10 are taken from the IFS and have been interpolated on the LITOS flight path.

The deep-fold case reveals a degenerate tripole structure with the lower positive peak being much weaker than the upper positive one. Maximum PV production rates are located about 10 K above the turbulent peak reaching 8 PVU h^{-1} (Figure 7a). The medium-fold case is dominated by a tripole structure with the negative pole located at the turbulent peak (Figure 7c). The maximum positive PV production rates are in the order of 0.2 PVU h^{-1}. Additionally, there is another tripole visible at a potential temperature level of 400 K, which is one order of magnitude weaker than the one below. It is caused by the turbulent peak around 14 km altitude (above the LS front) and will not be discussed further (c.f. Section 4.1). The degeneration of the tripole structure in the deep-fold case occurs, because the sharp lower boundary of the dissipation rate peak in combination with strongly changing static stability at the lower end of the peak minimized the lower positive peak of the PV production function.

Figures 7b and 7d show PV from the IFS on an isentropic coordinate interpolated on the LITOS flight path. In the extratropics, a steady increase of PV with potential temperature is expected (e.g., Hoskins, 1997). However, the IFS shows a different altitude profile of PV along the LITOS flight path: For both cases, we find a tripole structured deviation in PV around the tropopause. It consists of a local maximum above the turbulent peak reaching about 15 PVU (5 PVU) above the background for the deep (medium) tropopause fold case. Furthermore, there is a local minimum around the height of the jet core reaching tropospheric PV values and a second local maximum at the height of the stratospheric intrusion.

These anomalies in the PV profiles can be caused by turbulence induced PV tendencies as well as by the ageostrophic circulation around the jet. If they are thought to be caused by turbulence alone, one can estimate their development times from the ratio of the PV difference and the PV tendency. This suggests development times of about one hour in the deep-fold case and more than 24 h in the medium-fold case. The implications of these values will be discussed in Section 6.

From an NWP study using backward trajectories in the IFS, Spreitzer et al. (2019) also obtained a PV tripole structure caused by turbulence in the vicinity of UT and LS fronts. They see turbulent PV production rates up to 0.2 PVU h^{-1} (their Figure 7). This corresponds well to our values from the medium-fold case, but is more than one order of magnitude lower compared to the deep-fold case.

In another backward trajectory study using the Met Office Unified Model, Chagnon and Gray (2015) analyzed the net diabatic PV change around the tropopause regardless of the underlying process. They retrieved mean PV production rates of 0.03 PVU h^{-1} over an interval of 36 h (their Figure 3c) and found a dipole structure in PV around the tropopause, similar to our deep-fold case.

Similarly, Saffin et al. (2017) found a turbulence induced PV dipole structure across the tropopause. In their NWP study, they observed PV dipoles of about ±0.1 PVU for ridges. However, this is an average using three months of forecast. Accordingly, the absolute value can hardly be compared to our case study.

Concerning our measured turbulent PV modification distribution (Figures 7a and 7c) and the PV profile in the IFS (Figures 7b and 7d), we find different vertical extents of the tripoles: while the upper peak in our observed turbulent PV production is at the same potential temperature as the upper local peak seen in the IFS, the minimum and the lower peak in the IFS are extended to lower potential temperature.

In short, the observed PV tendencies match results obtained from model studies even though details are different. This is probably the case, because our observed turbulence distribution is different to the classical picture given by Shapiro (1976). For further discussion, please see Section 6.

5.4. Tracer Mixing Across the Tropopause Fold

In Figure 8, we show tracer-tracer correlations of water vapor and ozone to identify tropospheric and stratospheric as well as mixed air masses across the tropopause fold similar to several aircraft-based case studies (e.g., Gettelman et al., 2011). In contrast to those instruments the LITOS system measures humidity but cannot retrieve other trace gases. Therefore, we correlate water vapor measurements with ozone values from IFS data interpolated to the LITOS flight path.

Following recent publications, we define tropospheric air masses as being characterized by $H_2O > 12$ ppmv and $O_3 < 67$ ppbv and stratospheric air masses by $H_2O < 12$ ppmv and $O_3 > 67$ ppbv (Gettelman et al., 2011; Pan et al., 2007; Woiwode et al., 2018). Consequently, mixed air masses are identified by $H_2O \geq 12$ ppmv and $O_3 \geq 67$ ppbv.

For the deep-fold case we find almost no mixed air masses. The dissipation rate peak is almost entirely located in the stratospheric air mass, while a small portion is in the tropospheric air mass (inset of Figure 8a). Therefore, this combination of measurement and forecast data does not reveal any mixing that has happened before the sounding. The intrusion partly contains mixed air masses, albeit with comparatively low water vapor of $H_2O \leq 30$ ppmv.

For the medium-fold case the picture is entirely different (Figure 8b). The turbulent peak is partly located in stratospheric and partly in mixed air masses. The altitude band between the middle of the turbulent peak and the lower edge of the stratospheric intrusion is completely mixed. Compared to other tropopause fold studies such as Pan et al. (2007) and Woiwode et al. (2018) and the cases presented by Gettelman et al. (2011), our medium-fold case shows higher water vapor abundance in the mixed region.

6. Discussion

In this section, we relate our results to experimental as well as modeling studies on turbulence measurements and tropopause folds. In doing so, we focus on five main aspects:

- Techniques of the dissipation rate measurement
- Classification of measured dissipation rate values
- Geophysical interpretation of dissipation profiles across tropopause folds
- Turbulence induced PV tendencies
- Tracer-tracer correlations across the tropopause fold

Our method of retrieving dissipation rates relies on retrieving the Taylor microscale. The advantage in comparison to other techniques is that we do not rely on a complicated calibration of the instrument (e.g., Barat, 1982). Furthermore, we only use spatial scales between a few centimeters and 2 m, thereby avoiding influences from self-induced balloon motions (Scoggins, 1965; Söder, 2019). On the other hand, our instrument requires a higher signal-to-noise ratio due to the low magnitude of the velocity fluctuations at small scales (e.g., Söder et al., 2019).

The deep-fold case shows peak dissipation rates as large as 1,000 mW kg^{-1}. This is the highest atmospheric energy dissipation rate measured with the LITOS instrument so far. The value corresponds to severe turbulence according to ICAO (2018). Their limits for *light*, *medium*, and *severe* turbulence as represented by color shading in Figure 4 are similar to those from Sharman et al. (2014) that have been obtained for medium sized aircraft. The value of 1,000 mW kg^{-1} measured by LITOS is about half an order of magnitude larger than the highest bin in the statistics for commercial aircraft by Sharman et al. (2014, their Figure 10). Applying a 2 km vertical smoothing, for example, reduces the measured dissipation rate peak to 100 mW kg^{-1}. This underlines that high spatial resolutions are required to measure large dissipation rates caused by small-scale turbulent structures in the tropopause fold.

Regarding the medium-fold case, the LS front reveals dissipation rates of approximately 10 mW kg^{-1}, which is similar to former measurements performed in the UT front (Kennedy & Shapiro, 1975; Reid & Vaughan, 2004). The dissipation in the UT front of our deep-fold case is comparable to Cho et al. (1999, 3 mW kg^{-1}). Therefore, we conclude that our measured dissipation strengths are comparable to others except the LS front of the deep-fold case, which shows exceptionally large dissipation rates (1,000 mW kg^{-1}). Overall, a high level of turbulence was found as expected from the large-scale evolution of a breaking Rossby wave with far northern extend, a prominent jet streak and a deep tropopause fold.

More remarkable than the absolute energy dissipation rate is our measured turbulence distribution across the tropopause fold: in both cases the dissipation rate in the LS front is about three orders of magnitude larger than in the UT front. This is related to the Richardson numbers from our measurement: both cases show lower *Ri* in the LS front. Unfortunately, this can only be compared to one further measurement from

Kennedy and Shapiro (1980), which shows the opposite distribution compared to our case: weak dissipation rates were found in both the LS front and the UT front, with slightly larger values in the UT front. All other discussed measurements sounded the UT front only.

From the time evolution of the Richardson number as observed in the IFS, we find that on shorter time scales of a few hours, gradients increased in the UT front of the deep-fold case after the measurement (Figure S5). Contrarily, they decreased in both fronts for the medium-fold case (Figure S6). According to Lang and Martin (2012), this is a hint for a measurement in a comparatively early stage of the frontal development and matches the measured turbulence distribution in the deep-fold case. However, this comparison does neither match the turbulence distribution nor the measured *Ri* distribution for the medium-fold case, in contrast to *Ri* from the IFS. Therefore, it highlights the need for more turbulence soundings, especially in the LS front. Another issue is the understanding of turbulence and its dependence on environmental conditions. We find a weak relation of enhanced dissipation with low *Ri*, but this does not explain changes in dissipation rate by several orders of magnitude. A direct comparison of dissipation rates with *Ri* would require an estimate of mixing lengths, which is not available from the LITOS instrument. Hence, more observations are needed in combination with Lagrangian diagnostics for a complete account of the three-dimensional evolution of tropopause folds. This seems relevant, not least because these large dissipation rates are a potential hazard to high flying passenger aircraft and need to be reliably predicted (Bramberger et al., 2017; Koch et al., 2005; Sharman et al., 2012).

The importance of turbulence induced PV changes in tropopause fold generation as proposed by Shapiro (1976) has been confirmed by several model studies (Saffin et al., 2017; Shapiro, 1981; Spreitzer et al., 2019). Spreitzer et al. (2019) are able to assign PV modifications to physical processes parameterized in the IFS. They conclude that PV modifications on the stratospheric side of the tropopause fold are mainly driven by shear induced turbulence, while cloud and convective processes had the largest impact on the tropospheric side. This matches our observational findings: due to the lack of significant cloud-related convection, there is hardly any turbulence in the UT front (clear sky conditions in the vicinity of both LITOS soundings, data not shown here). This furthermore agrees with other observational turbulence studies in tropopause folds: Cho et al. (1999) and Reid and Vaughan (2004) observed cloud related convective turbulence in the UT front.

Regarding the tripole shape of the turbulence induced modification, our results confirm the IFS study by Spreitzer et al. (2019). Also the magnitude of our calculated PV tripole in the medium-fold case agrees well with their findings. For the deep-fold case however, the expected tripole has been deformed by the asymmetric shape of the dissipation peak: strong gradients from above but weaker gradients from below. Therefore, it looks similar to a dipole. Furthermore, we find PV tendencies one and a half orders of magnitude larger than in the medium-fold case.

This is partly explained by the strength of our ULJF: we see PV deviations of about 15 PVU in the IFS for our deep-fold case. This is one order of magnitude larger than the total PV change of about 1.5 PVU found for the relevant region by Spreitzer et al. (2019, their Figure 7). Nevertheless, a time frame of only two hours for the observed PV changes to be created seems small. Therefore, we assume that the dissipation rate has lowered at a later stage in the frontal development, possibly induced by turbulence driven weakening of the wind shear gradients. Unfortunately, this cannot be further affirmed, because a series of LITOS measurements through tropopause folds is not available yet and a parcel backtracing analysis of the IFS data as done by Spreitzer et al. (2019) would be outside the scope of this experimental study.

However, we like to point out that PV modifications do not only occur due to irreversible heating by turbulent dissipation, but also due to reversible advection. Such processes can be indirectly seen in the PV data of the medium fold case: The vertical extent of the tripole in the IFS is larger compared to what is expected from the turbulence induced PV tendencies. This hints on PV advection by other processes acting remote from the point of observation.

Nevertheless, our study provides observational evidence for the importance of turbulence to the PV structure in tropopause folds. Despite the low dissipation rates in both UT fronts sounded with LITOS, the observed PV production functions of the turbulent zones in the LS front alone can explain the magnitude of the PV deviations observed in the IFS.

Generally, we obtain PV changes from energy dissipation rate using a fixed flux Richardson number of $R_f = 0.15$ and neglecting frictional heating due to turbulence. From Zilitinkevich et al. (2008) we assume that the fixed flux Richardson number results in a heat flux error of smaller than a factor of two for $Ri > 0.1$ (as fulfilled in our measurement, Figure 5). Furthermore, our calculation of PV tendencies neglects the influence of frictional heating due to turbulent dissipation. This is done in accordance with Shapiro (1976), who neglects all diabatic and frictional processes in his calculations. Our measurements suggest that frictional turbulent heating is smaller than eddy flux heating by a factor of three at least. The PV tendency is changed by 25% at most (data not shown). As our consideration of PV tendencies is only used to assess the order of magnitude, we keep both approximations for simplicity.

Our tracer-tracer correlation for the medium-fold case shows that tropospheric and stratospheric air masses are well mixed from the lowermost part of the stratospheric intrusion up to the turbulent peak in the LS front. Such structures have been observed before in aircraft based studies of tropopause folds (Pan et al., 2007; Ungermann et al., 2013; Woiwode et al., 2018). The observed mixing is even more remarkable, as there was no significant turbulence present in the lower UT front, which could have two possible reasons: First, turbulence might have existed in the UT front before and decayed before the sounding took place. Second, the fine scale mixing may have primarily happened in the LS front and the mixed air masses been advected to the lower altitudes by the ageostrophic circulation around the jet. This hypothesis is supported by Ungermann et al. (2013) and Woiwode et al. (2018) finding narrow filaments in their trace gas distributions within the stratospheric intrusion, thereby pointing to the importance of advective processes in forming the stratospheric intrusion.

The tracer-tracer correlation for the deep-fold case on the other hand shows hardly any sign of mixing. This could eventually be a consequence of our observation taking place early in the ULJF life cycle with *Ri* still lowering in the IFS (Lang & Martin, 2012). However, this cannot be more than a hint, as Figure 5a reveals that the IFS severely overestimates the measured relative humidity in this altitude region as found by other studies (Kaufmann et al., 2018; Woiwode et al., 2020). Possibly, also the ozone concentrations from the IFS used for the tracer-tracer correlation could be compromised. Therefore, combining LITOS with an ozone sonde seems a worthwhile task for future field campaigns.

7. Conclusions

In this study, we used the ability of the LITOS instrument for high-resolution turbulence soundings within tropopause folds. It allows us to evaluate two continuous vertical dissipation rate profiles: one through a deep and one through a medium tropopause fold. Both where part of upper-level jet-front systems located on the eastern side of a ridge above central Europe.

In the two cases, dissipation rates in the shear zone above the upper-level jet were about three orders of magnitude larger compared to the shear zone below the jet. They reached 1,000 mW kg^{-1} in the deep and 10 mW kg^{-1} in the medium-fold case, corresponding to severe and moderate turbulence intensities. These turbulence levels correspond very well to the development state of the baroclinic Rossby wave and the depth of the tropopause fold.

The observed vertical structure of turbulence intensities matches with lower Richardson numbers measured by the radiosonde in the lower stratospheric (LS) front compared to the upper tropospheric (UT) front. For the deep-fold case, this is also seen in the integrated forecast system (IFS). However, it is not seen in the IFS for the medium-fold case due to an underestimation of the upper-level jet.

The observed dissipation rate peaks in the LS frontal zone are shown to cause a dipole (tripole) structured PV modification in the deep (medium) tropopause fold case. Their absolute values correspond well to numerical weather prediction studies in the literature, while they are about one order of magnitude larger in the deep-fold case. This difference may be caused by the high spatiotemporal variability of turbulence, which may not be fully resolved in operational weather forecasts.

Tracer-tracer correlations revealed a well-mixed transition layer in the medium-fold case, despite the lack of turbulence in the UT front. This may be interpreted as advective transport of mixed air from the LS front

into the stratospheric intrusion. For the deep-fold case, hardly any mixing was found from this analysis. This points out the need for combined turbulence—trace gas measurements to avoid using forecast data for this method.

Coming back to our research question on observational evidence for the turbulence pattern assumed by Shapiro (1976): In contrast to the general picture, we find turbulence to be mainly constrained to the LS front. However, our observations quantitatively confirm their picture of turbulent PV modification (Equation 10). Furthermore, they are in accordance with recent observational and numerical studies on PV modification and tracer fluctuations in tropopause folds. This may be taken as a hint that even in cases where meteorological forecasts suggest turbulence to occur equally above and below the jet in a tropopause fold, the real situation can be much different. Therefore, our understanding of the meteorological situation is expected to benefit from further observational studies, which might also explore possible implications for aviation safety.

Data Availability Statement

Data shown in the plots of this article are available online at https://doi.org/10.22000/332 (license CC BY 4.0). Data from the IFS can be obtained at https://www.ecmwf.int/. Raw data processing software for the LITOS instrument and the radiosonde is available on request to the corresponding author.

Acknowledgments
The corresponding author is grateful to the German Research Foundation (DFG) for support through the research unit Multi-Scale Dynamics of Gravity Waves (FOR 1898, "MS-GWaves") under the project PACOG (KL 611/25-2). C. Zülicke received partial funding from the same research group under the project Spontaneous Imbalance (ZU 120/2-2). Furthermore, we owe gratitude to Reik Ostermann and Michael Priester for technical support with the LITOS instrument, especially during the campaign phases. Moreover, we are thankful to Dale Lawrence and collaborators for their contribution to the campaign on January 19, 2020. The ECMWF IFS data have been kindly retrieved by Gerd Baumgarten. Last but not least, we like to thank three anonymous referees and the editor William Randel for their insightful comments and support during the review process. Open access funding enabled and organized by Projekt DEAL.

References

Attivissimo, F., Savino, M., & Trotta, A. (2000). A study on nonlinear averagings to perform the characterization of power spectral density estimation algorithms. *IEEE Transactions on Instrumentation and Measurement*, *49*(5), 1036–1042.

Barat, J. (1982). Some characteristics of clear-air turbulence in the middle stratosphere. *Journal of the Atmospheric Sciences*, *39*(11), 2553–2564. https://doi.org/10.1175/1520-0469(1982)039⟨2553:SCOCAT⟩2.0.CO;2

Bjerknes, J. (1937). Investigations of selected European cyclones by means of serial ascents. *Geofysiske Publikasjoner*, *12*(2), 3–18. Retrieved from https://ci.nii.ac.jp/naid/10009665785/en/

Bramberger, M., Dörnbrack, A., Bossert, K., Ehard, B., Fritts, D. C., Kaifler, B., et al. (2017). Does strong tropospheric forcing cause large-amplitude mesospheric gravity waves? A deepwave case study. *Journal of Geophysical Research: Atmospheres*, *122*, 11422–11443. https://agupubs.onlinelibrary.wiley.com/doi/abs/10.1002/2017JD027371

Bush, A. B. G., & Peltier, W. R. (1994). Tropopause folds and synoptic-scale baroclinic wave life cycles. *Journal of the Atmospheric Sciences*, *51*(12), 1581–1604. https://doi.org/10.1175/1520-0469(1994)051⟨1581:TFASSB⟩2.0.CO;2

Chagnon, J. M., & Gray, S. L. (2015). A diabatically generated potential vorticity structure near the extratropical tropopause in three simulated extratropical cyclones. *Monthly Weather Review*, *143*(6), 2337–2347. https://doi.org/10.1175/MWR-D-14-00092.1

Cho, J. Y. N., Newell, R. E., Bui, T. P., Browell, E. V., Fenn, M. A., Mahoney, M. J., et al. (1999). Observations of convective and dynamical instabilities in tropopause folds and their contribution to stratosphere-troposphere exchange. *Journal of Geophysical Research*, *104*(D17), 21549–21568. https://agupubs.onlinelibrary.wiley.com/doi/abs/10.1029/1999JD900430

Crameri, F., Shephard, G. E., & Heron, P. J. (2020). The misuse of color in science communication. *Nature Communications*, *11*(1), 5444. https://doi.org/10.1038/s41467-020-19160-7

Fritts, D. C., & Werne, J. A. (2013). Turbulence dynamics and mixing due to gravity waves in the lower and middle atmosphere. In D. E. Siskind, S. D. Eckermann, & M. E. Summers (Eds.), *Atmospheric science across the stratopause* (pp. 143–159). American Geophysical Union. https://doi.org/10.1029/GM123p0143

Gettelman, A., Hoor, P., Pan, L. L., Randel, W. J., Hegglin, M. I., & Birner, T. (2011). The extratropical upper troposphere and lower stratosphere. *Reviews of Geophysics*, *49*, RG3003. https://doi.org/10.1029/2011RG000355

Gidel, L. T., & Shapiro, M. A. (1979). The role of clear air turbulence in the production of potential vorticity in the vicinity of upper tropospheric jet stream-frontal systems. *Journal of the Atmospheric Sciences*, *36*(11), 2125–2138. https://doi.org/10.1175/1520-0469(1979)036⟨2125:TROCAT⟩2.0.CO;2

Hartjenstein, G. (2000). Diffusive decay of tropopause folds and the related cross-tropopause mass flux. *Monthly Weather Review*, *128*(8), 2958–2966. https://doi.org/10.1175/1520-0493(2000)128⟨2958:DDOTFA⟩2.0.CO;2

Heisenberg, W. (1948). Zur statistischen Theorie der Turbulenz. *Zeitschrift für Physik*, *124*(7-12), 628–657.

Hocking, W., & Mu, P. (1997). Upper and middle tropospheric kinetic energy dissipation rates from measurements of review of theories, in-situ investigations, and experimental studies using the Buckland Park atmospheric radar in Australia. *Journal of Atmospheric and Solar-Terrestrial Physics*, *59*(14), 1779–1803. https://doi.org/10.1016/S1364-6826(97)00020-5

Hoinka, K. P. (1997). The tropopause: Discovery, definition and demarcation. *Meteorologische Zeitschrift*, *6*(6), 281–303. http://doi.org/10.1127/metz/6/1997/281

Holton, J. R., Haynes, P. H., McIntyre, M. E., Douglass, A. R., Rood, R. B., & Pfister, L. (1995). Stratosphere-troposphere exchange. *Reviews of Geophysics*, *33*(4), 403–439. https://doi.org/10.1029/95RG02097

Hoskins, B. (1997). A potential vorticity view of synoptic development. *Meteorological Applications*, *4*(4), 325–334. https://doi.org/10.1017/S1350482797000716

Hoskins, B. J., McIntyre, M. E., & Robertson, A. W. (1985). On the use and significance of isentropic potential vorticity maps. *Quarterly Journal of the Royal Meteorological Society*, *111*(470), 877–946. https://doi.org/10.1002/qj.49711147002

ICAO. (2018). *Meeting of the meteorology panel (metp) fourth meeting (Tech. Rep. 4)*. International Civil Aviation Organization. Retrieved from https://www.icao.int/airnavigation/METP/Panel%20Meetings/METP4_Final%20Report.pdf

Jørgensen, F. E. (2005). *How to measure turbulence with hot-wire anemometers (Tech. Note)*. Dantec Dynamics A/S. Retrieved from https://web.iitd.ac.in/~pmvs/courses/mel705/hotwire2.pdf

Kaufmann, S., Voigt, C., Heller, R., Jurkat-Witschas, T., Krämer, M., Rolf, C., et al. (2018). Intercomparison of midlatitude tropospheric and lower-stratospheric water vapor measurements and comparison to ECMWF humidity data. *Atmospheric Chemistry and Physics*, *18*(22), 16729–16745. https://doi.org/10.5194/acp-18-16729-2018

Kennedy, P. J., & Shapiro, M. A. (1975). The energy budget in a clear air turbulence zone as observed by aircraft. *Monthly Weather Review*, *103*(7), 650–654. https://doi.org/10.1175/1520-0493(1975)103⟨0650:TEBIAC⟩2.0.CO;2

Kennedy, P. J., & Shapiro, M. A. (1980). Further encounters with clear air turbulence in research aircraft. *Journal of the Atmospheric Sciences*, *37*(5), 986–993. https://doi.org/10.1175/1520-0469(1980)037⟨0986:FEWCAT⟩2.0.CO;2

Keyser, D., & Shapiro, M. A. (1986). A review of the structure and dynamics of upper-level frontal zones. *Monthly Weather Review*, *114*(2), 452–499. https://doi.org/10.1175/1520-0493(1986)114⟨0452:AROTSA⟩2.0.CO;2

Koch, S. E., Jamison, B. D., Lu, C., Smith, T. L., Tollerud, E. I., Girz, C., et al. (2005). Turbulence and gravity waves within an upper-level front. *Journal of the Atmospheric Sciences*, *62*(11), 3885–3908. https://doi.org/10.1175/JAS3574.1

Kohma, M., Sato, K., Tomikawa, Y., Nishimura, K., & Sato, T. (2019). Estimate of turbulent energy dissipation rate from the vhf radar and radiosonde observations in the antarctic. *Journal of Geophysical Research: Atmospheres*, *124*, 2976–2993. https://doi.org/10.1029/2018JD029521

Kräuchi, A., Philipona, R., Romanens, G., Hurst, D. F., Hall, E. G., & Jordan, A. F. (2016). Controlled weather balloon ascents and descents for atmospheric research and climate monitoring. *Atmospheric Measurement Techniques*, *9*(3), 929–938. https://doi.org/10.5194/amt-9-929-2016

Lamarque, J.-F., & Hess, P. G. (1994). Cross-tropopause mass exchange and potential vorticity budget in a simulated tropopause folding. *Journal of the Atmospheric Sciences*, *51*(15), 2246–2269. https://doi.org/10.1175/1520-0469(1994)051⟨2246:CTMEAP⟩2.0.CO;2

Lang, A. A., & Martin, J. E. (2012). The structure and evolution of lower stratospheric frontal zones. Part 1: Examples in northwesterly and southwesterly flow. *Quarterly Journal of the Royal Meteorological Society*, *138*(666), 1350–1365. https://doi.org/10.1002/qj.843

Li, J. D. (2004). Dynamic response of constant temperature hot-wire system in turbulence velocity measurements. *Measurement Science and Technology*, *15*(9), 1835–1847. https://doi.org/10.1088/0957-0233/15/9/022

Lilly, D., Waco, D., & Adelfang, S. (1974). Stratospheric mixing estimated from high-altitude turbulence measurements. *Journal of Applied Meteorology*, *13*(4), 488–493.

Lübken, F.-J. (1992). On the extraction of turbulent parameters from atmospheric density fluctuations. *Journal of Geophysical Research*, *97*(D18), 20385–20395. https://doi.org/10.1029/92JD01916

NOAA. (1976). *US standard atmosphere (Tech. Rep.)*. 76, 1562, NOAA-S/T.

Osborn, T. R. (1980). Estimates of the local rate of vertical diffusion from dissipation measurements. *Journal of Physical Oceanography*, *10*(1), 83–89. https://doi.org/10.1175/1520-0485(1980)010⟨0083:EOTLRO⟩2.0.CO;2

Pan, L. L., Bowman, K. P., Shapiro, M., Randel, W. J., Gao, R. S., Campos, T., et al. (2007). Chemical behavior of the tropopause observed during the stratosphere-troposphere analyses of regional transport experiment. *Journal of Geophysical Research*, *112*, D18110. https://doi.org/10.1029/2007JD008645

Reed, R. J., & Danielsen, E. F. (1958). Fronts in the vicinity of the tropopause. *Archiv für Meteorologie, Geophysik und Bioklimatologie, Series A, Meteorologie und Geophysik*, *11*(1), 1–17.

Reid, H. J., & Vaughan, G. (2004). Convective mixing in a tropopause fold. *Quarterly Journal of the Royal Meteorological Society*, *130*(599), 1195–1212. https://doi.org/10.1256/qj.03.21

Saffin, L., Gray, S. L., Methven, J., & Williams, K. D. (2017). Processes maintaining tropopause sharpness in numerical models. *Journal of Geophysical Research: Atmospheres*, *122*(18), 9611–9627. https://doi.org/10.1002/2017JD026879

Schneider, A. (2015). *In-situ turbulence observations in the stratospheric wind and temperature field* (Dissertation, Universität Rostock). Retrieved from https://www.iap-kborn.de/fileadmin/user_upload/MAIN-abteilung/optik/Forschung/Doktorarbeiten/Schneider-Diss-2015.pdf

Schneider, A., Wagner, J., Söder, J., Gerding, M., & Lübken, F.-J. (2017). Case study of wave breaking with high-resolution turbulence measurements with LITOS and WRF simulations. *Atmospheric Chemistry and Physics*, *17*(12), 7941–7954. https://doi.org/10.5194/acp-17-7941-2017

Scoggins, J. R. (1965). Spherical balloon wind sensor behavior. *Journal of Applied Meteorology*, *4*(1), 139–145. https://doi.org/10.1175/1520-0450(1965)004⟨0139:SBWSB⟩2.0.CO;2

Scoggins, J. R. (1967). *Sphere behavior and the measurement of wind profiles (Tech. Rep.)*. NASA. Retrieved from https://ntrs.nasa.gov/archive/nasa/casi.ntrs.nasa.gov/19670017960.pdf

Shapiro, M., & Keyser, D. (1990). Fronts, jet streams, and the tropopause. In C. W. Newton, & E. Holopainen (Eds.), *Extratropical cyclones*. (pp. 167–191). American Meteorological Society.

Shapiro, M. A. (1974). A multiple structured frontal zone-jet stream system as revealed by meteorologically instrumented aircraft. *Monthly Weather Review*, *102*(3), 244–253. https://doi.org/10.1175/1520-0493(1974)102⟨0244:AMSFZJ⟩2.0.CO;2

Shapiro, M. A. (1976). The role of turbulent heat flux in the generation of potential vorticity in the vicinity of upper-level jet stream systems. *Monthly Weather Review*, *104*(7), 892–906. https://doi.org/10.1175/1520-0493(1976)104⟨0892:TROTHF⟩2.0.CO;2

Shapiro, M. A. (1980). Turbulent mixing within tropopause folds as a mechanism for the exchange of chemical constituents between the stratosphere and troposphere. *Journal of the Atmospheric Sciences*, *37*(5), 994–1004. https://doi.org/10.1175/1520-0469(1980)037⟨0994:TMWTFA⟩2.0.CO;2

Shapiro, M. A. (1981). Frontogenesis and geostrophically forced secondary circulations in the vicinity of jet stream-frontal zone systems. *Journal of the Atmospheric Sciences*, *38*(5), 954–973. https://doi.org/10.1175/1520-0469(1981)038⟨0954:FAGFSC⟩2.0.CO;2

Sharman, R., Cornman, L., Meymaris, G., Pearson, J., & Farrar, T. (2014). Description and derived climatologies of automated in situ eddy-dissipation-rate reports of atmospheric turbulence. *Journal of Applied Meteorology and Climatology*, *53*(6), 1416–1432.

Sharman, R., Trier, S., Lane, T., & Doyle, J. (2012). Sources and dynamics of turbulence in the upper troposphere and lower stratosphere: A review. *Geophysical Research Letters*, *39*, L12803. https://doi.org/10.1029/2012GL051996

Škerlak, B., Sprenger, M., Pfahl, S., Tyrlis, E., & Wernli, H. (2015). Tropopause folds in ERA-Interim: Global climatology and relation to extreme weather events. *Journal of Geophysical Research: Atmospheres*, *120*, 4860–4877. https://doi.org/10.1002/2014JD022787

Söder, J. (2019). *Turbulence observations on sounding balloons: Geophysical interpretations based on instrumental Revisions* (Doctoral dissertation). https://doi.org/10.18453/rosdok_id00002707

Söder, J., Gerding, M., Schneider, A., Dörnbrack, A., Wilms, H., Wagner, J., & Lübken, F.-J. (2019). Evaluation of wake influence on high-resolution balloon-sonde measurements. *Atmospheric Measurement Techniques*, *12*(8), 4191–4210. https://doi.org/10.5194/amt-12-4191-2019

Spreitzer, E., Attinger, R., Boettcher, M., Forbes, R., Wernli, H., & Joos, H. (2019). Modification of potential vorticity near the tropopause by nonconservative processes in the ECMWF model. *Journal of the Atmospheric Sciences*, *76*(6), 1709–1726. https://doi.org/10.1175/JAS-D-18-0295.1

Sprenger, M., Croci Maspoli, M., & Wernli, H. (2003). Tropopause folds and cross-tropopause exchange: A global investigation based upon ECMWF analyses for the time period March 2000 to February 2001. *Journal of Geophysical Research*, *108*(D12), 8518. https://doi.org/10.1029/2002JD002587

Stohl, A., Bonasoni, P., Cristofanelli, P., Collins, W., Feichter, J., Frank, A., et al. (2003). Stratosphere-troposphere exchange: A review, and what we have learned from staccato. *Journal of Geophysical Research: Atmospheres*, *108*(D12), 8516. https://doi.org/10.1029/2002JD002490

Strauss, L., Serafin, S., Haimov, S., & Grubišić, V. (2015). Turbulence in breaking mountain waves and atmospheric rotors estimated from airborne in situ and doppler radar measurements. *Quarterly Journal of the Royal Meteorological Society*, *141*(693), 3207–3225.

Survo, P., Turunen, M., Salo, T., & Jauhiainen, H. (2014). *Vaisala radiosonde rs41—New sensing technologies for operational upper air measurements*. Retrieved from https://www.wmo.int/pages/prog/www/IMOP/publications/IOM-116_TECO-2014/Session%201/O1_4_Survo_VaisalaRS41.pdf

Theuerkauf, A., Gerding, M., & Lübken, F.-J. (2011). LITOS—A new balloon-borne instrument for fine-scale turbulence soundings in the stratosphere. *Atmospheric Measurement Techniques*, *4*(1), 55–66. https://doi.org/10.5194/amt-4-55-2011

Tiefenau, H. K. E., & Gebbeken, A. (1989). Influence of meteorological balloons on temperature measurements with radiosondes: Nighttime cooling and daylight heating. *Journal of Atmospheric and Oceanic Technology*, *6*(1), 36–42. https://doi.org/10.1175/1520-0426(1989)006⟨0036:IOMBOT⟩2.0.CO;2

Ungermann, J., Pan, L. L., Kalicinsky, C., Olschewski, F., Knieling, P., Blank, J., et al. (2013). Filamentary structure in chemical tracer distributions near the subtropical jet following a wave breaking event. *Atmospheric Chemistry and Physics*, *13*(20), 10517–10534. https://doi.org/10.5194/acp-13-10517-2013

Vaisala (2018). *Vaisala radiosonde rs41-sg accuracy and reliability [Computer software manual]*. Retrieved from https://www.vaisala.com/sites/default/files/documents/RS41-SG-Datasheet-B211321EN.pdf

Werne, J., & Fritts, D. C. (1999). Stratified shear turbulence: Evolution and statistics. *Geophysical Research Letters*, *26*(4), 439–442. https://agupubs.onlinelibrary.wiley.com/doi/abs/10.1029/1999GL900022

WMO. (1957). Definition of the tropopause (Vol. *VI*, p. 136–137). Retrieved from https://library.wmo.int/doc\text{_}num.php?explnum\text{_}id=6960

Woiwode, W., Dörnbrack, A., Bramberger, M., Friedl-Vallon, F., Haenel, F., Höpfner, M., et al. (2018). Mesoscale fine structure of a tropopause fold over mountains. *Atmospheric Chemistry and Physics*, *18*(21), 15643–15667. https://doi.org/10.5194/acp-18-15643-2018

Woiwode, W., Dörnbrack, A., Polichtchouk, I., Johansson, S., Harvey, B., Höpfner, M., et al. (2020). Technical note: Lowermost-stratosphere moist bias in ECMWF IFS model diagnosed from airborne GLORIA observations during winter–spring 2016. *Atmospheric Chemistry and Physics*, *20*(23), 15379–15387. https://doi.org/10.5194/acp-20-15379-2020

Xie, F., Li, Y., Liu, Z., Wang, X., & Wang, L. (2017). A forced convection heat transfer correlation of rarefied gases cross-flowing over a circular cylinder. *Experimental Thermal and Fluid Science*, *80*, 327–336. https://doi.org/10.1016/j.expthermflusci.2016.09.002

Zhang, F. (2004). Generation of mesoscale gravity waves in upper-tropospheric jetfront systems. *Journal of the Atmospheric Sciences*, *61*(4), 440–457. https://doi.org/10.1175/1520-0469(2004)061⟨0440:GOMGWI⟩2.0.CO;2

Zilitinkevich, S. S., Elperin, T., Kleeorin, N., Rogachevskii, I., Esau, I., Mauritsen, T., & Miles, M. W. (2008). Turbulence energetics in stably stratified geophysical flows: Strong and weak mixing regimes. *Quarterly Journal of the Royal Meteorological Society*, *134*(633), 793–799. https://doi.org/10.1002/qj.264

Zülicke, C., & Peters, D. (2006). Simulation of inertia gravity waves in a poleward-breaking Rossby wave. *Journal of the Atmospheric Sciences*, *63*(12), 3253–3276. https://doi.org/10.1175/JAS3805.1

Zülicke, C., & Peters, D. (2008). Parameterization of strong stratospheric inertiagravity waves forced by Poleward-breaking Rossby waves. *Monthly Weather Review*, *136*(1), 98–119. https://doi.org/10.1175/2007MWR2060.1